Deriving percent crop cover over agriculture canopies using hyperspectral remote sensing

Article *in* Canadian Journal of Remote Sensing · June 2014

DOI: 10.5589/m07-064

4 authors, including:

Anna Pacheco
Agriculture and Agri-Food Canada
34 PUBLICATIONS **1,528** CITATIONS

SEE PROFILE

Bannari Abdou
Space Pix-Map International Inc.
138 PUBLICATIONS **2,814** CITATIONS

SEE PROFILE

Heather McNairn
Agriculture and Agri-Food Canada
269 PUBLICATIONS **6,710** CITATIONS

SEE PROFILE

Can. J. Remote Sensing, Vol. 34, Suppl. 1, pp. S110–S123, 2008

Deriving percent crop cover over agriculture canopies using hyperspectral remote sensing

A. Pacheco, A. Bannari, K. Staenz, and H. McNairn

Abstract. The objective of this study is to investigate the potential of hyperspectral remote sensing for providing green percent crop cover information over agricultural canopies for use in precision farming. Ground measurements and airborne hyperspectral Probe-1 data were acquired over two agricultural sites in July 1999 near Clinton, Ontario, Canada, and in July 2000 near Indian Head, Saskatchewan, Canada. A manual endmember selection and extraction approach was used to unmix the reflectance cubes. Linear constrained and weakly constrained unmixing was conducted to determine crop endmember fractions. Results indicate that the two spectral unmixing algorithms were equally successful. If prior knowledge of the fields exists, a manual endmember selection technique is a suitable approach for the selection of endmembers in an image scene. Correlations between ground data and Probe-1 crop fractions showed very good results (root mean square error (RMSE) of ±11.06% and ±11.20% and index of agreement (*D*) of 0.91 and 0.90 for constrained and weakly constrained unmixing, respectively) when the endmembers were adjusted for their impurity. This highlighted the importance of finding pure or the "purest" pixels for each endmember in the image scene. The use of spectral unmixing to quantify within-crop and within-field percent crop cover showed mixed success. Canola and wheat crops (RMSE of ±10.67% and ±11.77%; *D* of 0.94 and 0.85) revealed better correlations than the bean and corn crops (RMSE of ±10.83% and ±12.46%; *D* of 0.64 and 0.59). The somewhat poor results for pea crops (RMSE of ±9.70%; *D* of 0.58) are possibly due to the ground vertical photograph classification process where it was difficult to distinguish pea stems and residue components.

Résumé. L'objectif de cette étude est d'évaluer le potentiel de la télédétection hyperspectrale pour l'estimation du pourcentage du couvert des cultures agricoles pour une utilisation opérationnelle en agriculture de précision. Des mesures au sol (vérité terrain) et des données hyperspectrales aéroportées ont été acquises par le capteur Probe-1 au-dessus de deux sites agricoles en juillet 1999, près de Clinton (Ontario, Canada), et en juillet 2000, près de Indian Head (Saskatchewan, Canada). Une approche de sélection et d'extraction manuelle des composantes spectrales homogènes pures (endmember) a été utilisée pour l'extraction des fractions à partir des cubes de réflectances au sol. Deux modèles d'analyse de mixture spectrale linéaire (sous contrainte et sous faible contrainte) ont été utilisés pour dériver les fractions homogènes des cultures. Les résultats obtenus montrent que les deux algorithmes considérés permettent l'extraction de l'information avec la même efficacité et la même précision. En outre, si une connaissance a priori existe sur les champs agricoles lors du passage du capteur, la sélection manuelle des composantes spectrales homogènes pures constitue une approche adéquate pour la sélection et l'extraction de ces composantes pures directement de l'image. Pour des fins de validation, les corrélations entre les mesures au sol (vérité terrain) et les fractions de cultures dérivées des données images (Probe-1) ont montré globalement de très bons résultats (RMSE de ±11,06 % et ±11,20 %; et *D* de 0,91 et 0,90 pour la mixture spectrale sous contrainte et sous faible contrainte, respectivement), notamment lorsque les composantes spectrales homogènes pures ont été ajustées d'impureté. Ceci montre l'importance de trouver des pixels purs ou les « plus purs » pour chaque composante spectrale homogène de l'image. L'utilisation de l'analyse de mixture spectrale linéaire pour quantifier le pourcentage du couvert des cultures, soit à l'intérieur d'une même culture ou soit à l'intérieur d'un même champ, a montré des résultats partagés. Par exemple, les cultures du canola et du blé (RMSE de ±10,67 % et ±11,77 %; *D* de 0,94 et 0,85) ont affiché de meilleures corrélations que les cultures du haricot et du maïs (RMSE de ±10,83 % et ±12,46 %; *D* de 0,64 et 0,59). Quant aux cultures de petits pois, les résultats sont moins concluants (RMSE de ±9,70 %; *D* de 0.58), probablement à cause de la procédure de classification des photos verticales acquises au sol (vérité terrain pour la validation) où il a été difficile de distinguer entre les tiges des petits pois et les résidus de cultures.
[Traduit par la Rédaction]

Received 30 June 2005. Accepted 19 September 2005. Published on the *Canadian Journal of Remote Sensing* Web site at http://pubs.nrc-cnrc.gc.ca/cjrs on 16 June 2008.

A. Pacheco[1] and H. McNairn. Agriculture and Agri-Food Canada, 960 Carling Avenue, Ottawa, ON K1A 0C6, Canada.

A. Bannari. Remote Sensing and Geomatics of Environment Laboratory, Department of Geography, University of Ottawa, P.O. Box 450, Station A, Ottawa, ON K1N 6N5, Canada.

K. Staenz.[2] Canada Centre for Remote Sensing, Natural Resources Canada, 588 Booth Street, Ottawa, ON K1A 0Y7, Canada.

[1]Corresponding author (e-mail: pachecoa@agr.gc.ca).
[2]Present address: Alberta Terrestrial Imaging Centre, 401, 817-4th Avenue S., Lethbridge, AB T1J 0P3, Canada.

Introduction

The field of remote sensing has progressed considerably during the last two decades, and technological advances have allowed the simultaneous acquisition of images in hundreds of narrow contiguous bands in specific regions of the electromagnetic spectrum (Adams et al., 1993), such as the visible and near-infrared (VNIR), short-wave infrared (SWIR), and thermal infrared or a combination thereof (Edwards et al., 1991). This technology offers numerous possibilities for vegetation management in agriculture applications to discriminate between vegetation types and quantify and map various biochemical parameters, such as lignin, cellulose, nitrogen, and phosphorus, and numerous biophysical components, such as green percent crop cover, leaf area index, hydric stress, and productivity (Staenz et al., 1998b; Goetz, 1992). The advent of hyperspectral remote sensing also requires new analytical approaches and techniques, such as spectral mixture analysis (SMA) and spectral angle mapper image classification, to manipulate and process data and extract information from hundreds of spectral bands at a time (Goetz et al., 1985; Staenz, 1992).

Each pixel within a hyperspectral data cube provides a single spectrum, which generally represents a mixture of materials. The spectrum is influenced by the spectral properties of the mix of the components and the relationship between the major geophysical, biophysical, and chemical properties of the surface and the hyperspectral remotely sensed data (Tompkins et al., 1997). SMA assumes that the source of the spectral signature from a pixel is produced by more than one spectrally distinct component (Schwarz, 1998). The fundamental assumption of linear SMA is that generally each pixel on the surface is a physical mixture of several constituents weighted by the surface abundance, and the spectrum of the mixture is a linear combination of the endmember reflectance spectra.

Strahler et al. (1986) defined endmembers as "the features recognizable in a scene as being meaningful for an observer, and constitute abstractions of real objects that can be regarded as having uniform properties." Endmember selection is the most important step to successfully unmix a reflectance data cube and produce valid fractional abundances of the study site. Improper endmember selection can lead to meaningless fraction maps, especially if the endmembers spectra are inaccurate in a physical sense (Tompkins et al., 1997). In general, the exact number and identification of the endmembers within a reflectance cube may be unknown, and thus interpretation of the fraction maps becomes a difficult task. This problem is further complicated because the selection of endmembers is highly influenced by the scale (spatial resolution) of the data, the scattering by surface components, or other factors such as illumination and viewing geometry. Selecting endmembers from vegetative imagery is even more difficult, since the spectral behaviour of the different vegetation types is very similar (Deguise et al., 1999). Operationally, it is very problematic to find "pure" pixels (i.e., completely covered by a single material) at even the spatial resolution of airborne sensors (~5 m) (McNairn et al., 2001; Pacheco et al., 2001; 2002).

The primary objective of this article is to investigate the potential of hyperspectral remote sensing data for providing green percent crop cover information over agricultural canopies for use in precision farming. This study also examines a specific approach to select and extract endmembers for spectral unmixing analysis and the potential of spectral unmixing analysis to derive an accurate percent crop cover map. Image and ground data collection methods are described followed by the various image data preprocessing methods, including radiometric and spectral calibration, surface reflectance retrieval, and image georeferencing. Data processing methods such as endmember selection and extraction and spectral mixture analysis are also described. Lastly, results and discussions of the relationship between percent crop cover values derived from the Probe-1 data and ground percent crop cover derived from vertical ground photographs are presented.

Materials

Study site

This study was carried out over two agricultural sites and two field campaigns: Clinton (43°40′N, 81°30′W) in southern Ontario, located 21 km east of Lake Huron, in the summer season of 1999; and Indian Head (50°32′N, 103°40′W) in southern Saskatchewan, situated 68 km east of Regina, in the summer season of 2000 (**Figure 1**). Three corn fields (*Zea mais* L.) and three white beans fields (*Phaseolus vulgaris* L.) of various sizes were selected for analysis at the Clinton study site. No treatments were applied within these fields. For the Indian Head study site, the fields used for validation purposes were located on a precision test farm of the Indian Head Agricultural Research Foundation (IHARF). Eight 12-ha fields were selected: four were seeded with wheat (*Triticum aestivum* L.), two with canola (*Brassica napus* L.), and two with peas (*Lathyrus aphaca* L.). To increase field variability, variable fertilizer treatments were applied to the wheat and canola fields, and variable-rate seeding treatments were performed in the pea fields.

Image data collection

Hyperspectral remote sensing data were acquired with the airborne Probe-1 hyperspectral sensor (ESSI Inc., 2001) on 7 July 1999 and 28 June 2000 over the Clinton and Indian Head sites, respectively. Probe-1 is a "whiskbroom-style" instrument that collects data in the cross-track direction by mechanical scanning and in the along-track direction by movement of the airborne platform. This sensor acquires upwelling radiance in 128 bands in the VNIR and SWIR regions of the electromagnetic spectrum. The at-sensor radiance is dispersed by four spectrographs onto four linear detector arrays with 32 bands each. This sensor covers a wavelength region from 437.9 to 2506.7 nm almost continuously, with small gaps in the

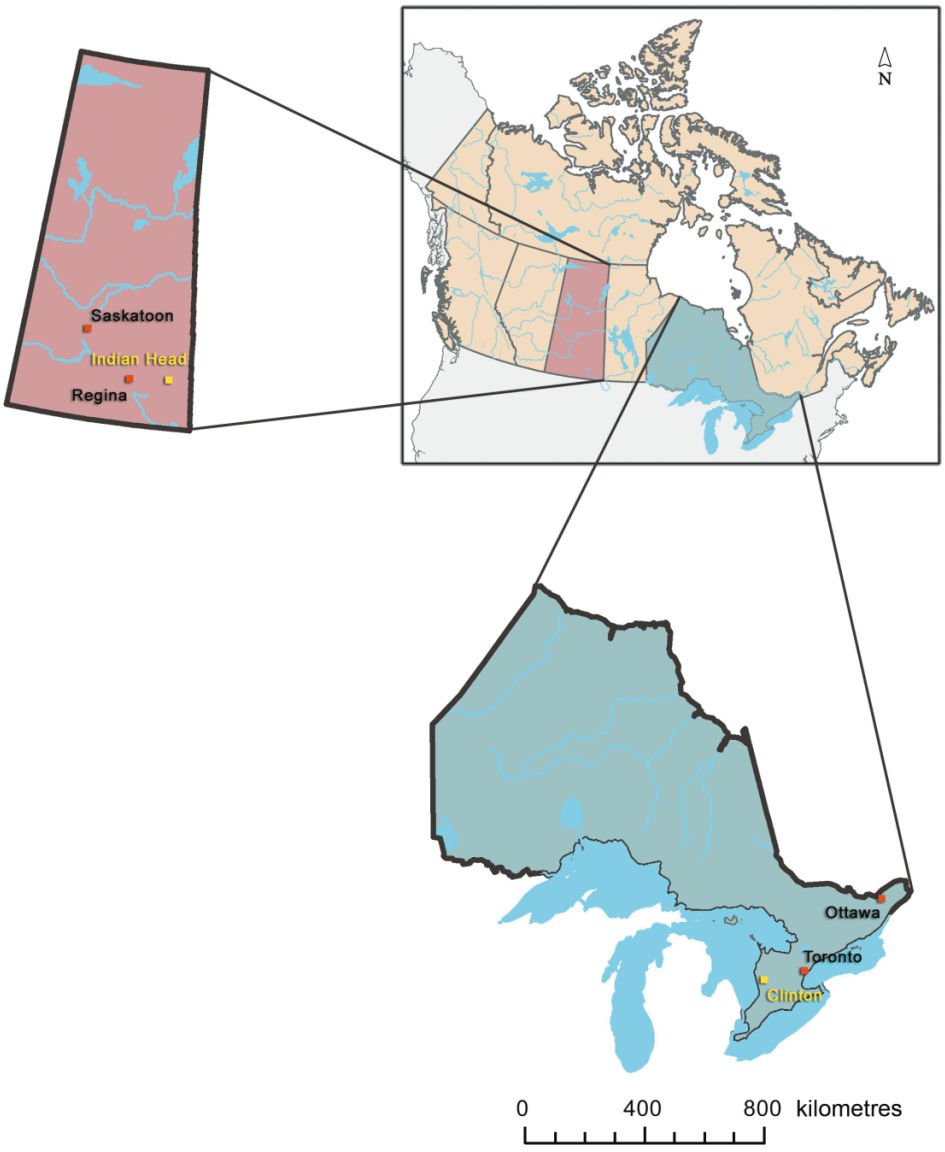

Figure 1. Location of Clinton and Indian Head study sites in Canada.

strong 1380 and 1870 nm atmospheric water vapour absorption. The bandwidths at full width half maximum (FWHM) vary from 13.3 to 22.3 nm, with a spectral sampling interval of 10.7–19.8 nm. The aircraft was flown at an altitude of around 2780 m above sea level, resulting in a swath width of 2.56 km (512 pixels) and a spatial resolution of about 5 m at nadir.

Ground data collection

In support of the airborne Probe-1 hyperspectral acquisitions, ground measurements were collected between 24 June and 7 July 1999 and between 2 and 4 July 2000 for the Clinton and Indian Head datasets, respectively. For the fields located in Clinton, approximately 10 sampling sites were selected per field to reflect within-field variability based on elevation and soil maps. A total of 60 sampling sites were marked with a flag, and the location of the flag was recorded with a differential global positioning system (GPS) unit. Due to the unavailability of pure pixels under natural field conditions, 20 m × 20 m patches of pure crop material were achieved by double seeding. Residue and bare soil were artificially created this way on four of the six fields. The location of each patch was measured with a differential GPS unit as well. These patches were used for the endmember selection process. For the fields located in Indian Head, a rectangular grid was overlaid on all the fields with an 80-m vertical and a 50-m horizontal spacing. Of the 308 points regularly distributed over the eight fields, only 96 points were selected for sampling purposes. These points were selected to cover within-field variability resulting from various nitrogen and variable-rate seeding treatments. The location of the 96 sampling sites was recorded in the same manner as that for Clinton. Similar to the Clinton

site, pure 20 m × 20 m patches of residue and soil were established in a field adjacent to the IHARF site.

Ground percent crop cover (PCC_G) data were calculated from vertical ground photographs taken at each sampling site and in each patch. These photographs were taken with a 35-mm camera equipped with a 28-mm lens. The camera was mounted on an overhead mast and used at a height of 2 m above ground. In this configuration, the camera viewed a ground area of about 4 m^2. Given that the Probe-1 data have a pixel size of 25 m^2, three photographs were acquired within 3–4 m of the centre of the sampling site locations for greater site representation.

Methods

Ground data preprocessing

The vertical ground photographs were digitized in three channels (blue, green, and red) and processed with ImageWorks (PCI Geomatics Enterprises Inc., 2000). Unsupervised classification was carried out using 10 classes: three classes for soil, three classes for leaf cover, two classes for residue, one class for soil shadow, and one class for leaf shadow. These classes were then aggregated to form three major components: leaf cover, residue, and soil. Once the classification was completed, percentages of leaf, soil, and residue cover were determined for each photograph by dividing the number of pixels for each component by the total number of pixels in the photograph. Final PCC_G was then calculated from the average of the three replicate photographs.

Image data preprocessing

Image data preprocessing was carried out using the imaging spectrometer data analysis system (ISDAS), a software package developed at the Canada Centre for Remote Sensing (CCRS) (Staenz et al., 1998a). The data preprocessing involved three components: radiometric calibration, spectral calibration, and surface reflectance retrieval.

Radiometric and spectral calibration

A laboratory calibration was completed for the Probe-1 sensor in April 1999 (Clinton dataset) and in April 2000 (Indian Head dataset) to obtain dark current signal and radiometric coefficients and to ascertain the centre position of the spectral bands. However, a vicarious calibration of the sensor was required to correct for errors in gains and band centres, which resulted from the stresses experienced during transportation, installation, and operation between the laboratory calibration and the overflight (Secker et al., 2001).

To achieve spectral calibration of the Probe-1 data, the raw spectrum (digital numbers) recorded by the sensor was converted to radiance using the radiometric gains and offsets derived in the laboratory. The derived radiance spectra were then analyzed to evaluate the wavelength and centre position of the band using five known atmospheric absorption features: 760 nm (oxygen), 940 and 1130 nm (water vapour), and 2005 and 2055 nm (carbon dioxide). Wavelength shifts were calculated, which best corrected the reflectance to obtain a smooth spectrum in the regions of these absorption features. These shifts were then applied to the Probe-1 data.

A reflectance-based vicarious calibration (RBVC) was then carried out using accurate ground-based reflectance measurements of specific targets at each study site. A 20 m × 20 m asphalt surface and a 5 m × 5 m bare soil patch were chosen as the calibration sites for Clinton and Indian Head, respectively. A portable GER-3700 field spectroradiometer (Geophysical and Environmental Research Corporation, 1990) was used to acquire ground-based reflectance measurements. This instrument measures radiance over a spectral range from 400 to 2500 nm using 704 spectral bands varying from 1.5 to 9.5 nm in width. Ground reflectance was calculated by ratioing target radiance to the radiance obtained from a calibrated white Spectralon panel (Labsphere, Inc., 2001). The Spectralon radiance was acquired immediately prior to the target radiance. The average of five spectra was convolved with Gaussian response profiles to match the bandwidths and band centres of the Probe-1 sensor. The calibration sites were then visually located in the Probe-1 imagery, and an average spectrum was computed for each target. The spectra from these targets were then matched to the averaged GER-3700 spectra. The differences between the two spectra were calculated, and the Probe-1 radiometric coefficients were adjusted to minimize the absolute reflectance difference until a 0.02% error threshold was reached. This process is computed in ISDAS using an iterative numerical technique, which provided a new set of gains after each iteration (Secker et al., 2001). The gains of the final iteration were then applied to the raw digital numbers to calculate at-sensor radiance for each dataset.

Surface reflectance retrieval

The calibrated at-sensor radiance data were converted to surface reflectance using a look-up-table (LUT) approach (Staenz and Williams, 1997). Two five-dimensional raw LUTs and one LUT for a 5% and 60% spectrally flat reflectance with tunable breakpoints were generated with a selected radiative transfer (RT) code to provide additive and multiplicative coefficients for the removal of scattering and atmospheric effects. The MODTRAN3 RT code was applied to the Clinton and Indian Head datasets using a mid-latitude summer atmosphere model and a continental-rural aerosol model, respectively. Other input parameters are listed in **Table 1**. The LUTs are then used in combination with a curve-fitting technique in the 940 and 1130 nm water vapour absorption regions to estimate the atmospheric water vapour content from the image data themselves on a pixel-by-pixel basis (Green et al., 1991; Gao and Goetz, 1990). The column atmospheric water vapour estimates were then interpolated using the LUTs to retrieve surface reflectance.

Image georeferencing

Airborne imagery generally contains considerable geometric distortion induced by the variations in the attitude of the aircraft during image acquisition. These attitude effects must be

Table 1. MODTRAN3 model input parameters for the atmospheric correction of the Probe-1 data.

Input parameter–dataset	Clinton 1999	Indian Head 2000
Date (year–month–day)	1999–07–07	2000–06–28
Greenwich Mean Time (GMT)	14:47:00	17:10:00
Aircraft heading (°)	180	110
Sensor altitude (m above sea level)	2778	2780
Terrain elevation (m above sea level)	340	579
Solar zenith angle (°)	39.68	34.35
Solar azimuth angle (°)	108.79	132.55
Atmospheric model	Mid-latitude summer	Mid-latitude summer
Aerosol model	Continental (rural)	Continental (rural)
Water vapour content (g/cm^2)	1.5	1.5
Ozone column (cm·atm (1 atm = 101.325 kPa); as per model)	0.319	0.319
CO_2 mixing ratio (ppm; as per model)	357.5	357.5
Horizontal visibility (km)	50	50

eliminated to ensure accurate correspondence between ground measurement locations and image pixel locations. A nondifferential GPS on board the aircraft registered the location of the aircraft during Probe-1 image acquisition, but unfortunately the system was not functional at the time of the data collection. As an alternative, high-spatial resolution orthophotos and 4-m orthorectified multispectral Ikonos imagery were used for the Clinton and Indian Head datasets, respectively, to establish sampling site locations via a reverse image-to-image registration technique. Sampling site locations were identified in the Probe-1 data by initially determining their location on the orthorectified image and then warping this image to match the Probe-1 imagery. This technique has the merit of preserving the radiometric integrity of each pixel in the Probe-1 imagery, given that the image pixels are not resampled.

The Clinton orthophotos were georeferenced to the Probe-1 image using 10 ground control points (GCPs) measured with a GPS (±1 m accuracy). These GCPs were then matched to pixels within the orthophotos with an accuracy of ±5 m or less. The Indian Head orthorectified Ikonos image was georeferenced to the Probe-1 image using 12 GCPs measured with a GPS (±1 m accuracy). Georeferencing was done using the same geodetic datum (WGS-84) to ensure ground sampling locations were compatible with image sampling locations. Lastly, the ground sampling locations were "burned" into the orthophotos and Ikonos image to ensure that the sampling site positions would remain visible once the orthorectified images were warped to the Probe-1 imagery.

The orthophotos and Ikonos ("slave") image were then coregistered to the Probe-1 imagery ("master") using first-, second-, or third-order polynomials in the GCP Works module of the PCI Geomatics Enterprises Inc. (2000) software. For each field in the Clinton dataset, 21–49 GCPs were identified on a visual basis at the corners of each field or at any other points clearly noticeable in both the slave and master images (i.e., intersections of rivers, roads, house corners, etc). Due to significant distortion of the Clinton hyperspectral imagery, a third-order polynomial fit was used for all fields. Eight to 20 GCPs were selected per field in the Indian Head dataset in both images, and only first- and second-order polynomial fits were applied to the data to achieve subpixel accuracy. Lastly, pixel and line coordinates from a 3 pixel by 3 pixel window centred on the sampling site were extracted from the warped orthophotos and IKONOS and retained for data extraction.

Image data processing

Endmember selection and extraction and spectral unmixing were applied to the surface reflectance data. The processing was done similarly for both datasets.

Endmember selection

A manual endmember extraction approach was used to select endmembers from the reflectance cube, from which endmember spectra are manually extracted based on prior knowledge of the fields. The endmember selection was carried out on an individual-field basis. For each field, two or three endmembers such as vegetation (crop), soil, and residue were identified and then extracted from the imagery for spectral unmixing purposes. However, not all fields contained residue, and this particular endmember was not included for spectral unmixing analysis for certain fields.

For the Clinton dataset, corn and white bean spectra were extracted from double-seeded 20 m × 20 m patches as the crop endmembers. Soil was also selected as an endmember for all fields, whereas only white bean fields contained residue. Soil and residue endmember spectra were also extracted from the image data within 20 m × 20 m pure patches containing these materials. In some instances, spectra were selected from various patches for one particular endmember and averaged for better representation of the actual field conditions. For the Indian Head dataset, five endmembers were selected and then extracted from the reflectance data. Endmembers included crop spectra of wheat, canola, peas, soil, and residue. Soil and residue endmembers were extracted from "patches" created in the northeast area of the IHARF site. Unfortunately, similar patches were not created for the crop endmembers (wheat, canola, and peas). However, a few days following the Probe-1

overflight, a quicklook image of the hyperspectral data was taken out in the field for validation purposes. Areas of high crop vigor were noted on the imagery, and the crop endmembers were then extracted directly from those areas of the imagery. A spectral array was then created containing each of the endmembers necessary for spectral unmixing analysis.

Spectral unmixing

Constrained and weakly constrained linear SMA was performed on both hyperspectral datasets using an algorithm implemented in ISDAS (Boardman, 1995; Shang et al., 2008). Constrained linear spectral unmixing is defined as follows:

$$\sum_{i=1}^{m} f_i = 1.0 \qquad 0 \le f_i \le 1 \tag{1}$$

where f_i is the fractional abundance of endmember i, and m is the total number of endmembers.

Weakly constrained linear spectral unmixing is a recently introduced option in ISDAS which relaxes the constraint that the fractions sum to one. If constrained linear spectral unmixing is performed on a data cube using an incomplete list of endmembers, the constrained unmixing algorithm will force the fraction of some of the pixels to get assigned to an inappropriate endmember, since the algorithm requires unit sum. The weakly constrained unmixing algorithm, however, allows the sum of fractions to be smaller than 1:

$$\sum_{i=1}^{m} f_i \le 1.0 \qquad 0 \le f_i \le 1 \tag{2}$$

The SMA was carried out using the full spectral range from 437.9 to 2506.7 nm, with the exception of the atmospheric water absorption regions located at 1380 and 1870 nm. Probe-1 reflectance cubes were unmixed on a field-by-field basis. Constrained unmixing generated for each field a crop and a soil fraction map, and a residue fraction map was produced for specific fields only (those containing residue). Weakly constrained unmixing generated the same fraction maps as constrained unmixing, with an additional fraction map from the reflectance contribution that was not assigned to the crop, soil, or residue endmembers. These fraction maps determine the relative contribution of each of the endmembers to the total reflectance recorded for each pixel, in which the values range from 0 to 1, where 0 indicates a low abundance and 1 a high abundance. Lastly, the percent crop cover (PCC) fraction maps were validated with the PCC_G derived from the classification of the ground vertical photographs.

Statistical analyses

Statistical analyses were carried out similarly for both the Clinton and Indian Head datasets. Statistical analyses were computed with the STATISTICA software (StatSoft, Inc., 1994). Various statistics were computed including means and standard deviations for both ground measurements (observed values) and image data (predicted values). Standard deviation statistics allowed the evaluation of data variability. This parameter was reported in all cases as an error percentage of the average value extracted from ground measurements (E_{PCC_G}) and the image data (E_{PCC_C}, E_{PCC_P}, $E_{PCC_{C\text{-}ADJ}}$, and $E_{PCC_{P\text{-}ADJ}}$). As for the spatial field variability within the imagery, errors were evaluated by computing average and maximum errors on a crop-by-crop and field-by-field basis. These errors were estimated from the set of error percentages calculated for each sampling of each individual crop type or field.

To validate image percent crop cover, ground measurements and image data values were compared using the 1:1 line. Ideally, observed and predicted values should have a correspondence of 1:1. An index of agreement, D, reflects the degree to which the observed value is accurately estimated by the predicted value. The index of agreement was calculated as follows (Willmott, 1982):

$$D = \left[\frac{\sum_{i=1}^{n} (P_i - O_i)^2}{\sum_{i=1}^{n} (|P_i'| + |O_i'|)^2} \right] \tag{3}$$

where P_i is the predicted value at sample i, O_i is the observed value at sample i, P_i' is the difference between P_i and the average of the predicted values, O_i' is the difference between O_i and the average of the observed values, and n is the number of values. A perfect model would have a D value of 1.

The root mean square error (RMSE) was used as an additional measure to supplement the index of agreement described previously. This statistic also quantifies the relationship for models that should ideally have a 1:1 relationship between observed and predicted values. This error measure was calculated with the following equation (Wilmott, 1982):

$$\text{RMSE} = \sqrt{\frac{\sum_{i=1}^{n} (P_i - O_i)^2}{n}} \tag{4}$$

The RMSE indicates the magnitude of the average error produced by a model. This error is reported in the same units as those for the observed and predicted values. Scatterplots displaying observed and predicted variables were also generated as graphic aids in evaluating the relationship between the variables (Willmott, 1982).

The relationship between observed and predicted values was also analyzed using a linear regression model. The slope (a), intercept (b), and coefficient of determination (R^2) of the regression model were calculated and used to evaluate the strength of the linear relationship between observed and predicted values. Significance levels (p) were calculated for each correlation. Regression models rarely produce a scatterplot where all points fall on a regression line, with a slope of 1.0 and an intercept of 0.0. Therefore, these parameters

are fundamental to the statistical analysis of the regression model. Systematic linear overpredictions or underpredictions generate characteristic variations in the slope and intercept values, which can help to interpret the major sources of error. Correlations were run on data pooled from both datasets, for each crop type, and lastly for each individual field.

Results

Image registration and error analysis

The hyperspectral sensor flew twice over each study site, generating two images over each field. For the Clinton dataset, one pass was chosen per field to perform image registration. This was done based on visual assessment of the geometric integrity of each field for both passes. Pass 1 achieved better geometry for bean-1, corn-2, and corn-3, and pass 2 demonstrated a better fit for bean-2, bean-3, and corn-1 (**Table 2A**). A large number of GCPs were collected for each field of the Clinton dataset given that the fields were very large (~47–90 acres (1 acre = 0.405 ha)) compared with those at Indian Head. Generally, geometric registration aims for subpixel accuracy (i.e., when the RMSE is less than 1 pixel). This was achieved for most of the fields in both datasets (**Tables 2A**, **2B**). Fields corn-1 and corn-3 had higher RMSE values of 1.23 and 1.19, respectively, which are still acceptable errors.

In contrast with the Clinton dataset, selection of the overpass for the Indian Head dataset was done on a ground sampling site basis. Selection was mostly based on the geometric integrity of the fields, since RMSE values were comparable between passes for several fields (**Table 2B**). Image data for wheat-1 and pea-2 were selected from pass 1, and data for all the other fields were chosen from pass 2 (**Figure 2**). Similarly to Clinton, the polynomial warping for both passes of the Indian Head dataset resulted in a good fit, achieving an accuracy of less than a subpixel for all selected fields except wheat-1 and canola-2 (1.92 and 1.42, respectively), as shown in **Table 2B**. The large RMSE value (1.92) for wheat-1 (pass 1) can be attributed to the large geometric distortion surrounding sampling points 42 and 44. Consequently, image data for these sampling points only were derived from pass 2 (RMSE = 0.50), which preserved better geometric integrity of that area (**Figure 2**).

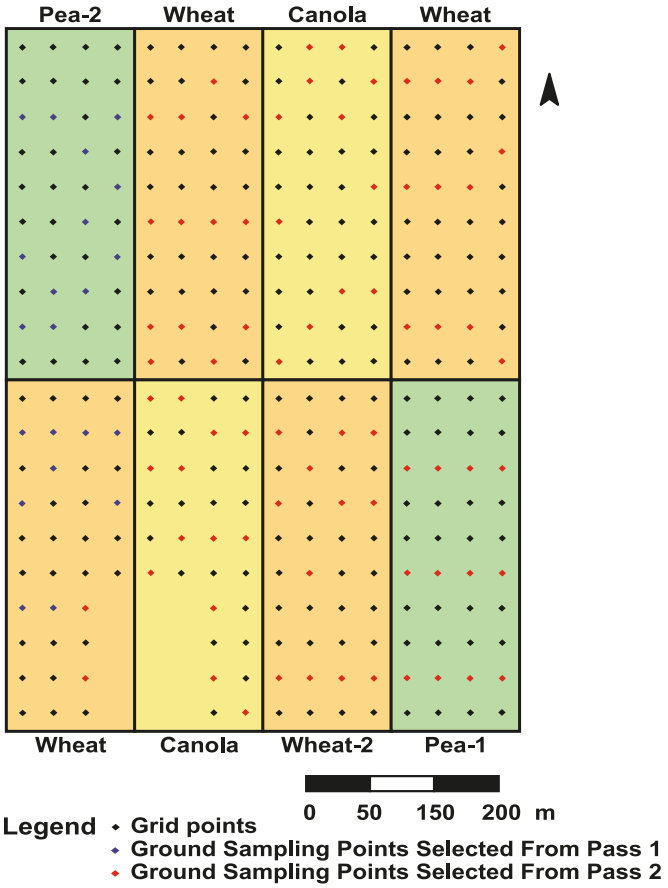

Figure 2. Sampling site selection for the Indian Head dataset.

Table 2. Results of image-to-image registration for Clinton field sites (where RMSE is for the polynomial fitting between the orthophotos and the Probe-1 imagery) and Indian Head field sites (where RMSE is for the polynomial fitting between the Ikonos imagery and the Probe-1 imagery).

(A) Clinton field sites

Field name	Selected pass	No. of GCPs	RMSE (pixels)
Bean-1	1	49	0.54
Bean-2	2	28	0.45
Bean-3	2	36	0.48
Corn-1	2	46	1.23
Corn-2	1	21	0.12
Corn-3	1	41	1.19

(B) Indian head field sites

	No. of GCPs		RMSE (pixels)	
Field name	Pass 1	Pass 2	Pass 1	Pass 2
Wheat-1	13	20	1.92	0.50
Wheat-2	10	8	0.25	0.49
Wheat-3	11	12	0.45	0.62
Wheat-4	12	16	0.19	0.27
Canola-1	12	14	0.45	0.50
Canola-2	10	11	1.42	0.73
Pea-1	10	12	0.27	0.27
Pea-2	11	10	0.22	0.74

Endmember selection and extraction

Figures 3a and **3b** illustrate the endmember spectra used for the SMA of the Clinton and Indian Head datasets, respectively. The residue spectrum is similar to the soil spectra in the VNIR region of the electromagnetic spectrum but differs considerably in the SWIR II region (2000–2400 nm). The specific absorption feature near 2100 nm that is characteristic of residue is noticeable in both figures. It can also be noted that the soil and residue spectra have a little trough at the chlorophyll well (~680 nm), indicating absorption of radiation and, consequently, the presence of some vegetation. This is due to the fact that the soil and residue spectra were slightly contaminated by vegetation for the Clinton dataset.

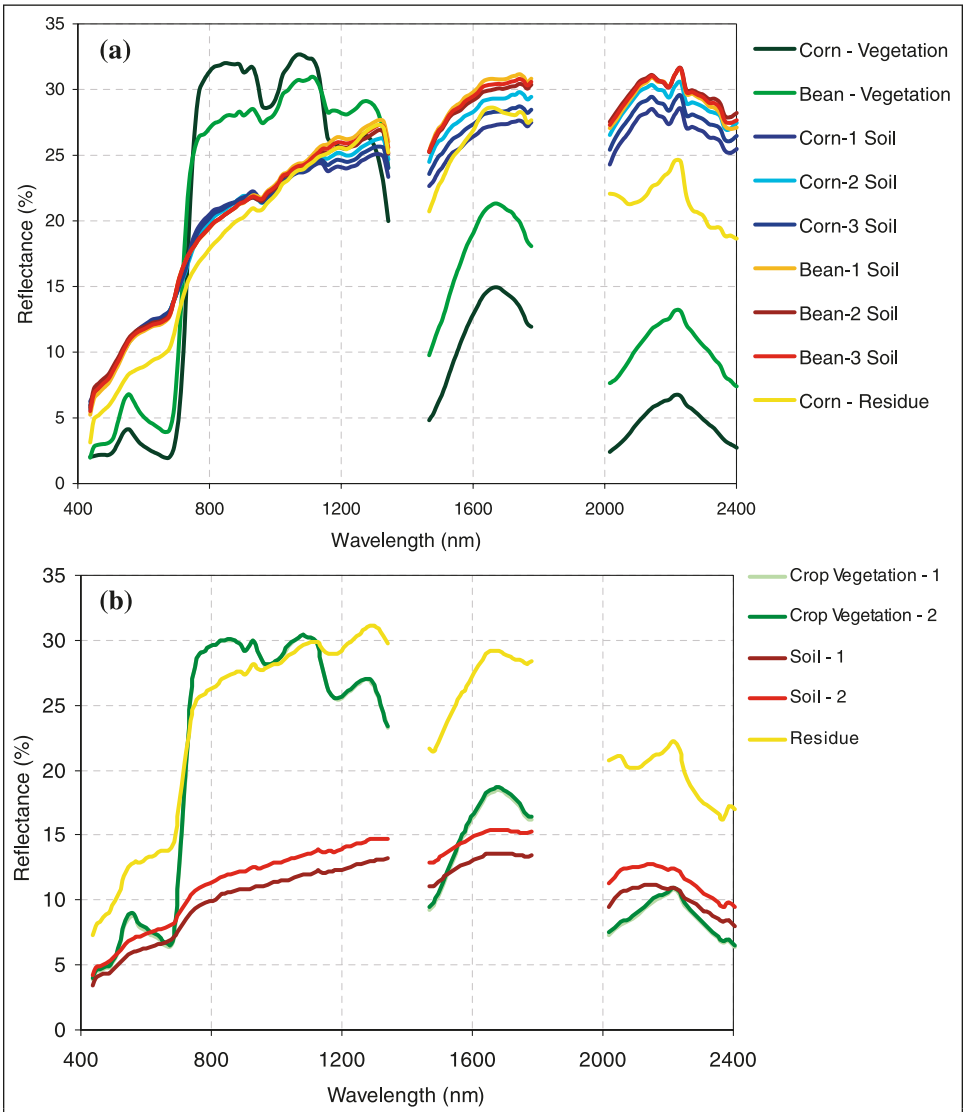

Figure 3. Average endmember spectra used for spectral unmixing analysis for (a) the Clinton dataset and (b) the Indian Head dataset. Gaps in the reflectance spectra are due to noisy bands, which were removed. In the legend for (b), the numbers 1 and 2 indicate endmember spectra extracted from pass 1 and pass 2, respectively.

Table 3. Fit statistics for PCC derived from the ground vertical photographs (PCC_G) and the reflectance data using constrained unmixing (PCC_C) and weakly constrained unmixing (PCC_P) for all crops.

(A) Constrained unmixing						
PCC_G (%)	PCC_C (%)	E_{PCC_G} (%)	E_{PCC_C} (%)	RMSE (±%)	D	R^2
49.42	66.55	18.01	9.53	23.04	0.72	0.52*
(B) Weakly constrained unmixing						
PCC_G (%)	PCC_P (%)	E_{PCC_G} (%)	E_{PCC_P} (%)	RMSE (±%)	D	R^2
49.42	65.08	18.01	9.67	21.90	0.73	0.51*

Note: a and b, slope and intercept, respectively, of the least squares regression line; D, index of agreement; E_{PCC_G}, E_{PCC_C}, and E_{PCC_P}, standard deviations as a percentage of the mean values; R^2, coefficient of determination; RMSE, root mean square error.

*Significant at $p < 0.05$.

This is also true for the residue spectra of the Indian Head dataset. Although this method of selecting and extracting endmembers has proven to be successful, it is subjective and, like other manual endmember extraction methods, no measure of error is available.

Spectral mixture analysis (SMA)

Linear SMA was conducted on all reflectance cubes for the Clinton and Indian Head datasets using the constrained and weakly constrained algorithms.

Constrained versus weakly constrained unmixing

Percent crop cover derived from constrained unmixing (PCC_C) and weakly constrained unmixing (PCC_P) were computed for all canopies of the Clinton and Indian Head reflectance datasets. When visually examining the crop fraction maps for the Clinton dataset, it can be noted that the weakly constrained unmixing method slightly decreased the crop fraction. This is mainly the case for corn canopies, where PCC_C was on average 94% and decreased to an average of 88% for PCC_P. It is also evident that there is not very much variability within the fields, especially for corn fields, where the PCC values cover a range of 9% on average. For Indian Head, the weakly constrained unmixing did not have as much effect on the reduction of the PCC compared with that for the Clinton dataset. Also, PCC variability within the fields is much larger for Indian Head due to the different nitrogen treatment applications on the fields.

Percent crop cover (PCC) validation

PCC values derived from the constrained and weakly constrained unmixing were validated against the percent crop cover estimated from ground vertical photographs (PCC_G). The relationship between the two variables was assessed on an agricultural canopy level (including all bean, corn, wheat, canola, and pea canopies). Statistics were generated from this relationship and are given in **Table 3A** for constrained unmixing and **Table 3B** for weakly constrained unmixing.

The correlations between PCC_G for all crops and both PCC_C ($D = 0.72$; $R^2 = 0.52$) and PCC_P ($D = 0.73$; $R^2 = 0.51$) were very similar. The RMSE values for both methods were also close to one another, with values of ±23.04% and ±21.90% for PCC_C and PCC_P, respectively. The scatterplots as shown in **Figure 4** also demonstrated the strong similarity of both relationships. Generally, the graphs reveal a linear relationship between the two variables, but the PCC values were consistently overestimating the ground observations, which results in data points not fitting the 1:1 line.

The consistent overestimation of the PCC measurements compared with the PCC_G measurements was caused by two reasons. The first is related to what the hyperspectral sensor actually "senses." When solar radiation penetrates through a vegetation canopy, the radiation is scattered and reflected, and its direction and spectral composition are transformed in a complex manner by the vegetation (Goel, 1988). The canopy reflectance is the sum of the reflectance of all vegetation components, such as leaves, stalks, stems, bark, and flowers. Accordingly, the hyperspectral sensor essentially measures spectral reflectance from the total volume of the canopy (McNairn et al., 2001), which includes the aforementioned components of the plant. The hyperspectral sensor measures PCC by incorporating the three-dimensional structure of the canopy, whereas the PCC_G values derived from the photographs can measure two-dimensional plant area (including leaves, stalks, stems). The PCC is a reflection of the actual vegetation amount in the canopy because it considers the

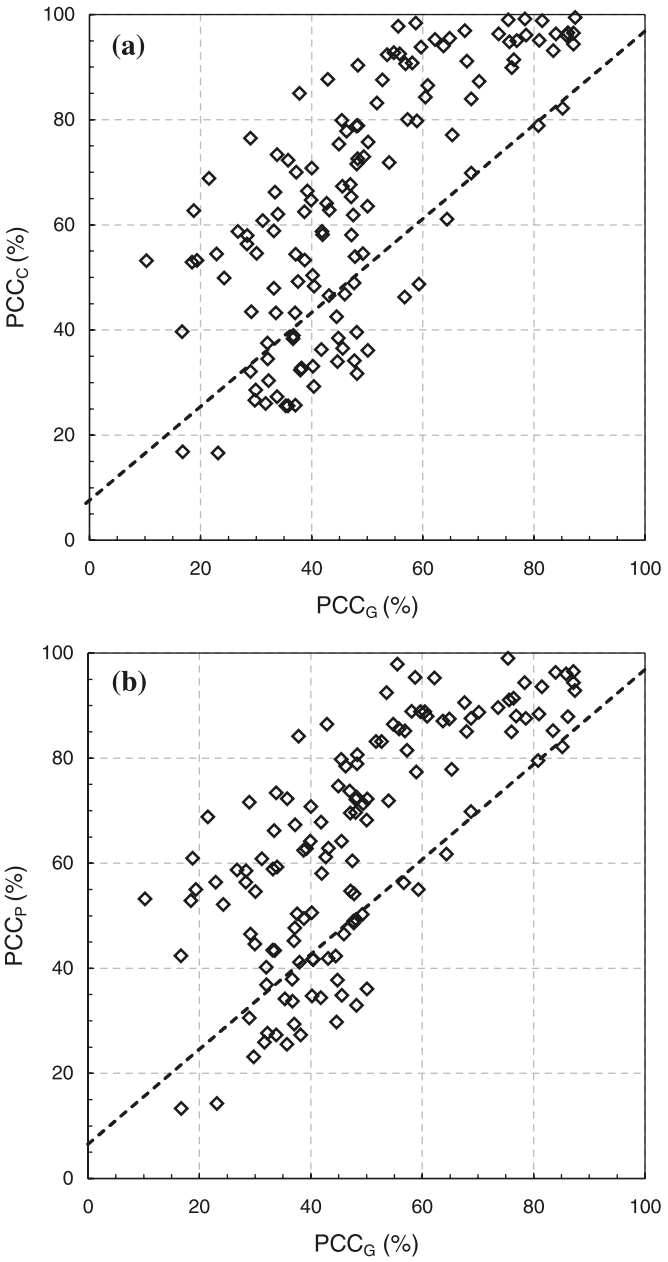

Figure 4. Relationship between PCC derived from the ground vertical photographs (PCC_G) and reflectance data using (a) constrained unmixing (PCC_C) and (b) weakly constrained unmixing (PCC_P) for all crops. The broken lines in **Figures 4–10** are the 1:1 line.

Table 4. Adjustment factor for each crop type.

Crop type	Adjustment factor
Bean	0.40
Corn	0.72
Wheat	0.82
Canola	0.83
Pea	0.80

total volume of the canopy, whereas the PCC_G is more representative of the true PCC of the canopy. Vegetation canopies can be represented by the same vegetation volume but have very different vegetation covers, and thus generate an error in the estimation of true PCC. Despite this error, the hyperspectral sensor was successful in estimating PCC.

The second reason is related to the endmember selection and extraction process. Pure patches were generated to minimize errors in selecting endmembers. Even though precautions were taken to avoid the contamination of pure patches, the examination of the endmember spectra revealed that the pure patches were not exactly pure. In Clinton, the crop patches were double-seeded to obtain full vegetation cover and thus enabled the extraction of a pure crop endmember. During the field campaign, it was evident that the pure crop patches were not 100% composed of vegetation and that the soil background was somewhat apparent. In Indian Head, the pure crop endmembers were extracted from high-density crop areas. The soil background was also apparent, and these areas were small in size and the reflectance from surrounding material (soil and residue) could have contributed to the contamination of the crop endmember spectra. Despite this problem, the crop endmembers were still selected from the purest pixels available in the reflectance cubes, and spectral unmixing analysis was carried out using two or three spectrally distinctive endmembers per field. This enabled reasonably good estimation of the PCC.

Percent crop cover (PCC) endmember "impurity" adjustment

An adjustment factor was introduced in the PCC computation to take into account the potential error associated with the impurity of the endmember. This factor was calculated for Clinton using the same procedure as that used for the estimation of PCC_G, where ground vertical photographs were identified for the crop patches. For Indian Head, endmembers were extracted in high-density crop growth areas using the Probe-1 imagery, as described in the Methods section. The field validation also included written observations, which visually assessed the PCC for the specific sites where endmembers were extracted. The "true" average PCC_G (averaged on a crop basis) was ratioed against the PCC values derived for each individual sampling site. Adjustment factors were then computed for each crop type and are presented in **Table 4**. Statistics derived from this adjustment with respect to the PCC_C and PCC_P values are given in **Table 5** and scatterplots shown in **Figure 5**.

The scatterplots depicting the relationship between the PCC_G and the adjusted crop fractions, derived from constrained ($PCC_{C\text{-}ADJ}$) and weakly constrained unmixing ($PCC_{P\text{-}ADJ}$), clearly illustrate a better fit to the 1:1 line than the unadjusted PCC (see **Figure 4**). **Table 5** indicates that *D* values increased considerably once the PCC values were adjusted for spectral impurity (from 0.72 to 0.91 for $PCC_{C\text{-}ADJ}$ and from 0.73 to 0.90 for $PCC_{P\text{-}ADJ}$). This was also reflected in the RMSE, which was reduced from ±23.04% and ±21.90% to ±11.06% and ±11.20% for $PCC_{C\text{-}ADJ}$ and $PCC_{P\text{-}ADJ}$, respectively. Average PCC values were much more comparable with $PCC_{C\text{-}ADJ}$ and $PCC_{P\text{-}ADJ}$ values. R^2 values also increased considerably from 0.52 and 0.51 to 0.71 and 0.69 for $PCC_{C\text{-}ADJ}$ and $PCC_{P\text{-}ADJ}$, respectively.

Both constrained and weakly constrained unmixing methods worked extremely well and are good predictors of PCC in agricultural canopies. For further analysis, however, only the $PCC_{P\text{-}ADJ}$ values are considered because this method relaxes the constraint that image fractions sum to one. This algorithm is much more lenient and recognizes that it is possible that not all endmembers were identified within the scene. In agriculture canopies, these endmembers could include shadow, weeds, pebbles, and water puddles. For example, a water puddle was present in the north area of the pea-5 field, and almost 50% of its pixels were contributing to the $PCC_{C\text{-}ADJ}$ values. However, when examining the $PCC_{P\text{-}ADJ}$ values, the reflectance contribution was reduced to almost 0%, indicating that the "weakly constrained unmixing" algorithm detected the water and classified it as being a different endmember than crop, soil, or residue. This can also be noted in the bean-1 reflectance cube where shadow was classified in the "other endmember"

Table 5. Fit statistics for PCC adjusted for endmember impurity for all crops derived from the ground vertical photographs (PCC_G) and the reflectance data using constrained unmixing ($PCC_{C\text{-}ADJ}$) and weakly constrained unmixing ($PCC_{P\text{-}ADJ}$).

(A) Constrained unmixing						
PCC_G (%)	$PCC_{C\text{-}ADJ}$ (%)	E_{PCC_G} (%)	$E_{PCC_{C\text{-}ADJ}}$ (%)	RMSE (±%)	*D*	R^2
49.42	46.86	18.01	9.53	11.06	0.91	0.71*
(B) Weakly constrained unmixing						
PCC_G (%)	$PCC_{P\text{-}ADJ}$ (%)	E_{PCC_G} (%)	$E_{PCC_{P\text{-}ADJ}}$ (%)	RMSE (±%)	*D*	R^2
49.42	45.84	18.01	9.67	11.20	0.90	0.69*

Note: $E_{PCC_{C\text{-}ADJ}}$ and $E_{PCC_{P\text{-}ADJ}}$, standard deviations as a percentage of the mean values.
*Significant at $p < 0.05$.

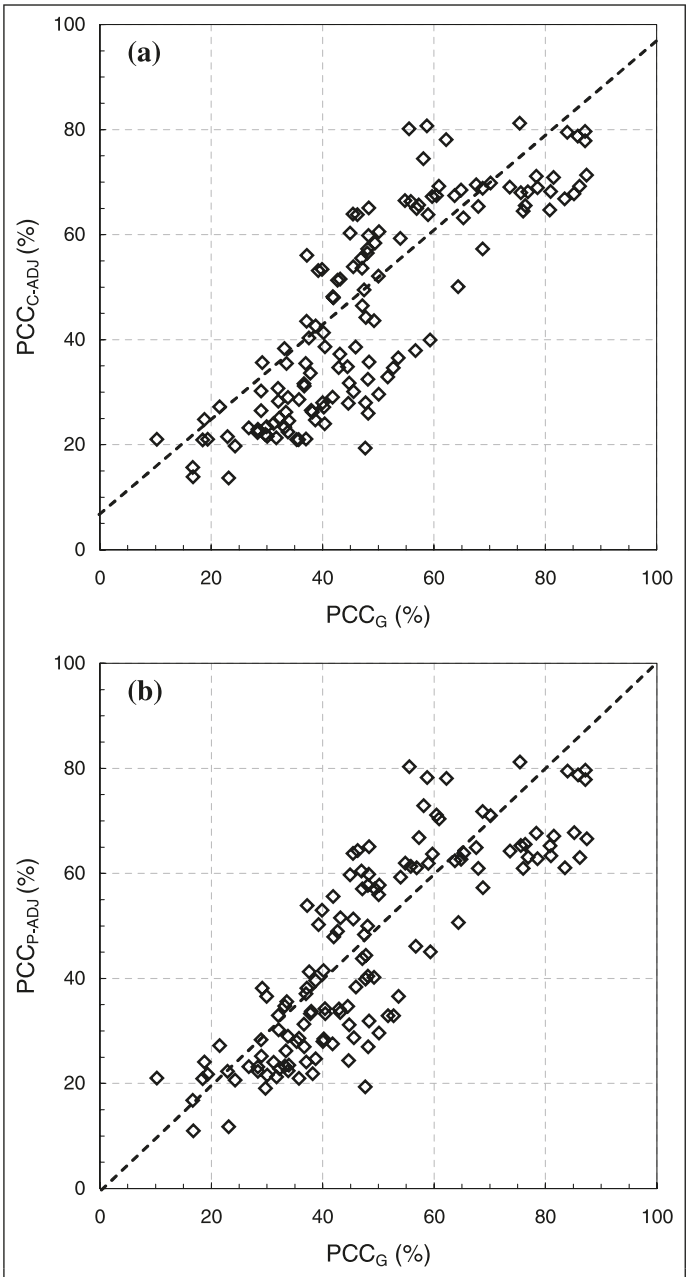

Figure 5. Relationship between PCC derived from the ground vertical photographs (PCC_G) and reflectance data using (a) constrained unmixing (PCC_{C-ADJ}) and (b) weakly constrained unmixing (PCC_{P-ADJ}) adjusted for endmember impurity for all crops.

fraction image when weakly constrained unmixing was used. Therefore, weakly constrained unmixing is a much better model to describe actual field conditions of vegetation canopies. To facilitate reading, PCC_{P-ADJ} is referred to as PCC_P from this point on.

Potential for modelling crop and field variability

For remote sensing models to retrieve plant biophysical parameters and to be efficient tools in precision agriculture, they must be able to detect within-crop and within-field variations that are of interest to the agriculture industry. The within-crop and within-field divergences of the percent crop cover are examined in this next section. The robustness of the models was evaluated for each individual crop type.

In regards to the PCC estimation (**Table 6**), the model was overall a very good predictor for wheat (D = 0.85) and canola (D = 0.94). The results were less satisfactory for beans (D = 0.64), corn (D = 0.59), and peas (D = 0.58). The wheat and canola fields revealed large crop cover variability (**Figures 6**, **7**), with the canola fields showing the largest variability. This is probably due to the different seeding dates for the two canola fields. Canola-2 was seeded 8 days prior to canola-1, producing a more phenologically developed crop with higher percent crop cover. The large variability within the wheat fields was most likely due to different seeding rates applied in the fields, resulting in different crop densities across the fields. According to **Figure 8**, pea fields also demonstrated a good variability in PCC as a result of different seeding rates within the fields. Although the index of agreement was relatively low (D = 0.58) for peas, the RMSE value was the best among all crops studied (RMSE = 9.70%).

The predicted model values for beans and corn had a weaker linear relationship with the PCC_G (**Figures 9**, **10**). RMSE values were somewhat similar to those of the other canopies, but D values were much lower than those in canola and wheat fields. The lower variability range in the data for the bean and corn fields studied can to some extent explain this poorer relationship. The variability range in the PCC_G was lower in the bean (45%) and corn (40%) fields compared with the average variability within the other crops (56%). This was especially the case for the image data values where variability was no more than 20% compared with an average variability of 60% for the other crops. The bean and corn fields were more homogeneous as a result of the absence of applied treatments,

Table 6. Fit statistics for PCC derived from the ground vertical photographs (PCC_G) and image using weakly constrained unmixing (PCC_P) on a within-crop basis.

Field	PCC_G (%)	PCC_P (%)	E_{PCC_G} (%)	E_{PCC_P} (%)	RMSE (±%)	D	R^2
Bean	32.48	25.78	15.19	3.96	10.83	0.64	0.52*
Corn	71.16	62.85	8.16	2.27	12.46	0.59	0.38*
Wheat	48.53	47.17	14.61	6.67	11.77	0.85	0.59*
Canola	48.86	44.96	38.07	28.99	10.67	0.94	0.81*
Pea	46.09	48.45	14.03	6.46	9.70	0.58	0.58*

*Significant at $p < 0.05$.

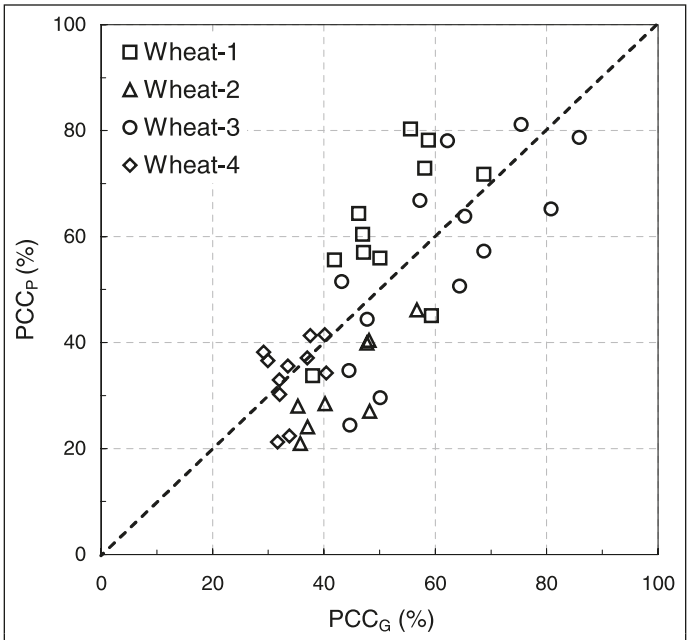

Figure 6. Relationship between PCC derived from the ground vertical photographs (PCC_G) and reflectance data using weakly constrained unmixing (PCC_P) for wheat fields.

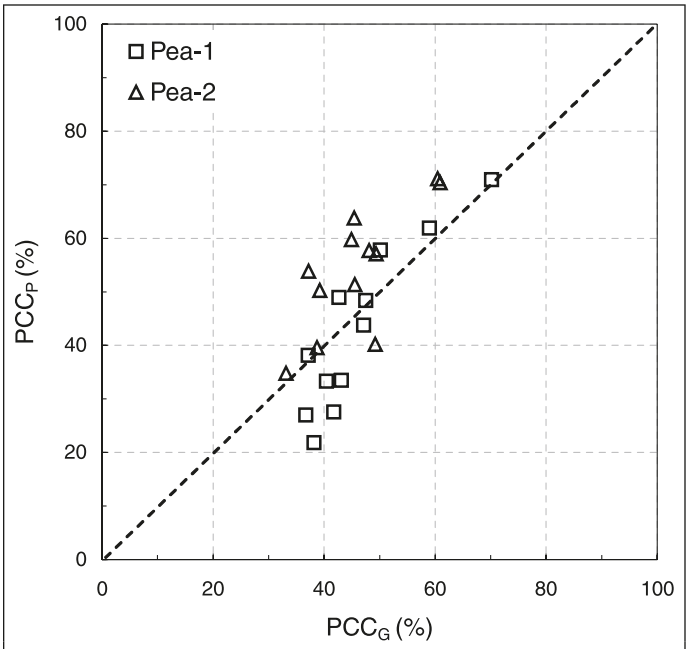

Figure 8. Relationship between PCC derived from the ground vertical photographs (PCC_G) and reflectance data using weakly constrained unmixing (PCC_P) for pea fields.

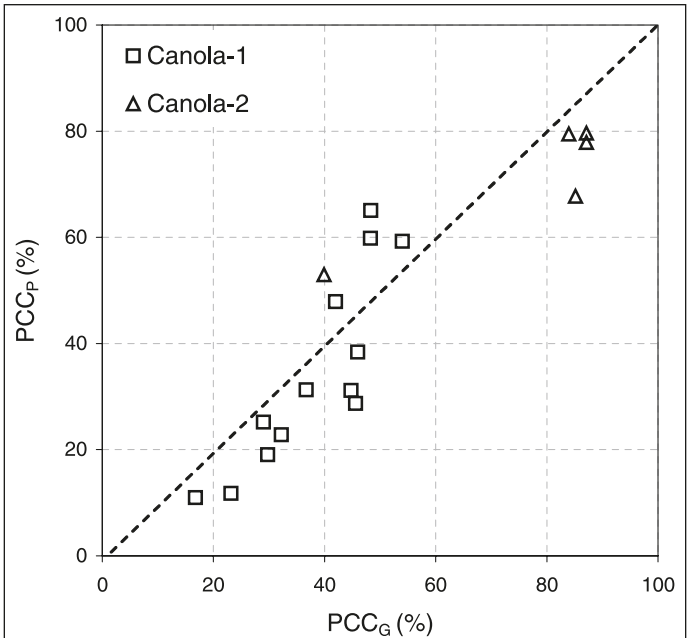

Figure 7. Relationship between PCC derived from the ground vertical photographs (PCC_G) and reflectance data using weakly constrained unmixing (PCC_P) for canola fields.

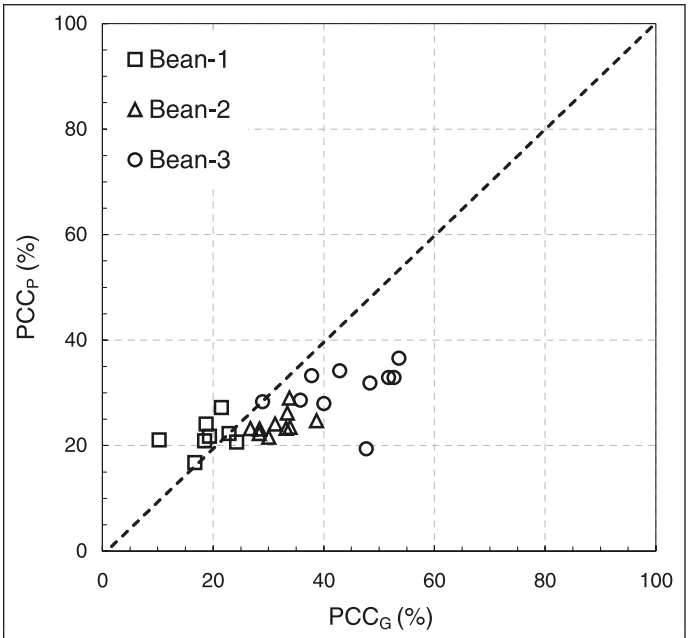

Figure 9. Relationship between PCC derived from the ground vertical photographs (PCC_G) and reflectance data using weakly constrained unmixing (PCC_P) for bean fields.

unlike the fields in Indian Head, where the various treatment applications artificially increased intrafield variability. Generally, the model to estimate PCC was sensitive to a limited range of variability.

A closer examination of the individual field results led to a few observations. High *D* values (>0.73) and relatively low RMSE (~10.00%) characterized the results for the pea fields. Low variability of PCC values within fields explained the poorer results found in the bean and corn canopies. *D* values were relatively close to 0.45 for beans, whereas these differed significantly within the three corn fields. Corn-3 had a *D* value of 0.61 compared with 0.28 for corn-2. The extremely low variability within corn-2 (error percentage = 5.83) explains the low *D* value. Once again, the seeding-rate treatments in the

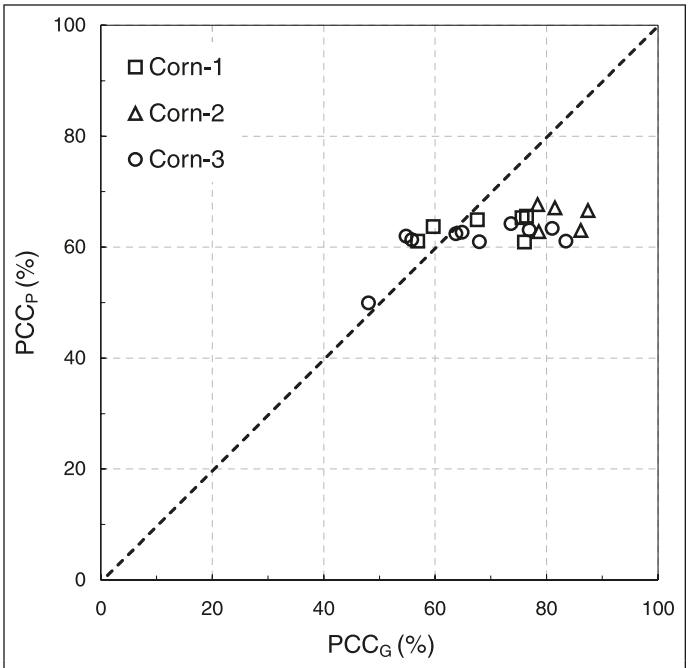

Figure 10. Relationship between PCC derived from the ground vertical photographs (PCC_G) and reflectance data using weakly constrained unmixing (PCC_P) for corn fields.

fields of the Indian Head dataset were an important factor, increasing the variability within each field. Moreover, image acquisition and ground data acquisition differed slightly in time, and that could have contributed to the discrepancy in the results, especially with the Clinton dataset where sudden growth occurred between the two acquisitions due to rainfall.

Summary and conclusions

The use of the spectral unmixing technique employed in this study proved to be quite efficient for estimating ground percent crop cover (PCC_G). The effect of the impurity of endmembers on the spectral unmixing analysis was revealed when crop fractions were adjusted for pixel impurity. Adjusting the crop fractions increased the *D* values from 0.72 to 0.91 and decreased the root mean square error (RMSE) from ±23.04% to ±11.06% in estimating percent crop cover for all crops using constrained unmixing. It also increased the *D* values from 0.73 to 0.90 and decreased the RMSE from ±21.90% to ±11.20% for the weakly constrained unmixing. The results indicate that the two spectral unmixing algorithms were equally successful. This suggests that the endmember spectra, selected within the reflectance cube itself, were really representative of the field conditions. Thus, the contribution of other small components (e.g., shadow) was very minimal and does not influence the results to a significant level. This finding is important because it simplifies the endmember selection and extraction process by eliminating the crop shadow influence on the spectral unmixing analysis. The results also show that the manual endmember extraction technique is appropriate for endmember selection and extraction when endmembers are known and can be well identified in the hyperspectral image.

The use of the spectral unmixing technique to quantify within-crop and within-field PCC showed mixed success. The PCC model was sensitive to the high variability in the canola (*D* = 0.94; RMSE = ±10.67%) and wheat crops (*D* = 0.85; RMSE = ±11.77%). However, this level of variability was somewhat artificial, since the crops were subject to variable-rate treatments. This is evident in the results for corn and beans, in which the model was not as sensitive to the level of variability found in beans (*D* = 0.64; RMSE = ±10.83%) and corn (*D* = 0.59; RMSE = ±12.46%) under ambient field conditions. The somewhat poor results for pea crops (*D* = 0.58; RMSE = ±9.70%) are possibly due to the classification process used for the ground vertical photographs where pea stems and residue were difficult to distinguish.

Acknowledgments

This research was carried out as part of a master's thesis project at the University of Ottawa, and the authors would like to thank the University of Ottawa Faculty of Graduate and Postdoctoral Studies and the Natural Sciences and Engineering Research Council of Canada (NSERC) for their financial support. The authors would also like to acknowledge the Canada Centre for Remote Sensing (CCRS), Natural Resources Canada, which provided the data. We would like to thank numerous people who were involved in this project and who provided their support and expertise: Jean-Claude Deguise (CCRS), Catherine Champagne (MIR Télédétection Inc.), Jiali Shang (University of Waterloo), Dr. Peter White (CCRS), Christian Nadeau (MacDonald, Detwiller and Associates Ltd.), Rob Hitchcock (Prologic Systems), and Lixin Sun (Dendron Resource Surveys Inc.), and all the field teams at Clinton and Indian Head.

References

Adams, J.B., Smith, M.O., and Gillepsie, A.R. 1993. Imaging spectroscopy: interpretation based on spectral mixture analysis. In *Remote geochemical analysis: elemental and mineralogical composition*. Edited by C.M. Pieters and P.A.J. Englert. Cambridge University Press, Cambridge, Mass. pp. 145–166.

Boardman, J.W. 1995. Analysis, understanding and visualization of hyperspectral data convex sets in N-Space. In *Proceedings of the International SPIE Symposium on Imaging Spectrometry*, 12–13 May 1995, Orlando, Fla. Edited by M.R. Descour, J.M. Mooney, D.L. Perry, and L.R. Illing. Proceedings of SPIE Volume 2480, pp. 14–20.

Deguise, J.-C., Staenz, K., and Lefebvre, J. 1999. Agricultural applications of airborne hyperspectral data: weed detection. In *Proceedings of the 4th International Airborne Remote Sensing Conference and Exhibition and the 21st Canadian Symposium on Remote Sensing*, 21–24 June 1999, Ottawa, Ont. Vol. 2, pp. 352–358.

Edwards, G., Jaton, A., and Thomson, K.P.B. 1991. La manipulation des données hyperspectrales. *Télédétection et Gestion des Ressources*, Vol. 7, pp. 295–299.

ESSI Inc. 2001. *About Probe-1*. EarthSearch Sciences Inc. (ESSI Inc.), Lakeside, Mont. Available from earthsearch.com/technology.

Gao, B.C., and Goetz, A.F.H. 1990. Column atmospheric water vapor and vegetation liquid water retrieval from airborne imaging spectrometer data. *Journal of Geophysical Research*, Vol. 95, pp. 3549–3564.

Geophysical and Environmental Research Corporation. 1990. *GER-3700 spectroradiometer user's manual, version 2.1*. Geophysical and Environmental Research Corporation, Millbrook, N.Y. 55 pp.

Goel, N.S. 1988. Models of vegetation canopy reflectance and their use in estimation of biophysical parameters from reflectance data. *Remote Sensing Reviews*, Vol. 4, No. 1, pp. 16–25.

Goetz, A.F.H. 1992. Imaging spectrometry for earth observations. *Episodes*, Vol. 15, No. 1, pp. 7–14.

Goetz, A.F.H., Vane, G., Solomon, J.E., and Rock, B.N. 1985. Imaging spectrometry for earth remote sensing. *Science (Washington, D.C.)*, Vol. 228, No. 4704, pp. 1147–1153.

Green, R.O., Conel, J.E., Margolis, J.S., Brugge, C.J., and Hoover, G.L. 1991. An inversion algorithm for the retrieval of atmospheric and leaf water absorption from AVIRIS radiance with compensation for atmospheric scattering. In *Proceedings of the 3rd Annual Airborne Visible/Infrared Imaging Spectrometer (AVIRIS) Workshop*, 20–21 May 1991, Pasadena, Calif. Jet Propulsion Laboratory (JPL), Pasadena, Calif. Publication JPL-91-28, pp. 51–61.

Labsphere, Inc. 2001. *A guide to reflectance coatings and materials*. Labsphere, Inc., North Sutton, N.H. Available from www.labsphere.com/tech_info/docs/Coating_&_Material_Guide.pdf.

McNairn, H., Deguise, J.C., Pacheco, A., Shang, J., and Rabe, N. 2001. Estimation of crop cover and chlorophyll from hyperspectral remote sensing. In *Proceedings of the 23rd Canadian Remote Sensing Symposium*, 21–24 August 2001, Saint-Foy, Que. CD-ROM. Canadian Aeronautics and Space Institute (CASI), Ottawa, Ont.

Pacheco, A., Bannari, A., Deguise, J.-C., McNairn, H., and Staenz, K. 2001. Application of hyperspectral remote sensing for LAI estimation in precision farming. In *Proceedings of the 23rd Canadian Remote Sensing Symposium*, 21–24 August 2001, Saint-Foy, Que. CD-ROM. Canadian Aeronautics and Space Institute (CASI), Ottawa, Ont. Vol. 1, pp. 281–287.

Pacheco, A., Bannari, A., Staenz, K., McNairn, H., and Deguise, J.-C. 2002. Validating LAI using hyperspectral imagery over agricultural canopies. In *Proceedings of the 1st International Symposium on Recent Advances in Quantitative Remote Sensing*, 16–20 September 2002, Torrent, Valencia, Spain. pp. 210–215.

PCI Geomatics Enterprises Inc. 2000. *Using PCI software*. PCI Geomatics Enterprises Inc., Richmond Hill, Ont. 540 pp.

Secker, J., Staenz, K., Gauthier, R.P., and Budkewitsch, P. 2001. Vicarious calibration of airborne hyperspectral sensors in operational environments. *Remote Sensing of Environment*, Vol. 76, pp. 81–92.

Schwarz, J. 1998. *Classification of hyperspectral data*. M.Sc. thesis, School of Computer Science, Carleton University, Ottawa, Ont. 180 pp.

Secker, J., Staenz, K., Gauthier, R.P., and Budkewitsch, P. 2001. Vicarious calibration of airborne hyperspectral sensors in operational environments. *Remote Sensing of Environment*, Vol. 76, No. 1, pp. 81–92.

Shang, J., Neville, R., Staenz, K., Sun, L., Morris, B., and Howarth, P. 2008. Comparison of fully constrained and weakly constrained unmixing through mine-tailing composition mapping. *Canadian Journal of Remote Sensing*, Vol. 34, Suppl. 1, pp. S92–S109.

Staenz, K. 1992. A decade of imaging spectrometry in Canada. *Canadian Journal of Remote Sensing*, Vol. 18, No. 4, pp. 187–197.

Staenz, K., and Williams, D.J. 1997. Retrieval of surface reflectance from hyperspectral data using a look-up table approach. *Canadian Journal of Remote Sensing*, Vol. 23, No. 4, pp. 354–368.

Staenz, K., Szeredi, T., and Schwarz, J. 1998a. ISDAS — A system for processing/analyzing hyperspectral data. *Canadian Journal of Remote Sensing*, Vol. 24, No. 2, pp. 99–113.

Staenz, K., Deguise, J.-C., Chen, J.M., McNairn, H., Szeredi, T., and McGovern, M. 1998b. The use of hyperspectral data for precision farming. In *Proceedings of the ISPRS Commission VII Symposium on Resource and Environmental Monitoring*, 1–4 September 1998, Budapest, Hungary. Vol. 22, Part 7, pp. 38–42.

StatSoft, Inc. 1994. *STATISTICA for Windows, version 4.0*. StatSoft, Inc., Tulsa, Okla.

Strahler, A.H., Woodcock, C.E., and Smith, J.A. 1986. On the nature models in remote sensing. *Remote Sensing of Environment*, Vol. 20, pp. 121–139.

Tompkins, S., Mustard, J.F., Pieters, C.M., and Forsyth, D.W. 1997. Optimization of endmembers for spectral mixture analysis. *Remote Sensing of Environment*, Vol. 59, pp. 472–489.

Willmott, C.J. 1982. Some comments on the evaluation of model performance. *Bulletin of the American Meteorological Society*, Vol. 63, No. 11, pp. 1309–1313.